The Astrophysical Journal Supplement Series, 246:57 (10pp), 2020 February https://doi.org/10.3847/1538-4365/ab65bd

Density Fluctuations in the Solar Wind Based on Type III Radio Bursts Observed by *Parker Solar Probe*

Vratislav Krupar[1,2,3], Adam Szabo[2], Milan Maksimovic[4], Oksana Kruparova[3], Eduard P. Kontar[5], Laura A. Balmaceda[2,6], Xavier Bonnin[4], Stuart D. Bale[7,8,9,10], Marc Pulupa[8], David M. Malaspina[11], John W. Bonnell[8], Peter R. Harvey[8], Keith Goetz[12], Thierry Dudok de Wit[13], Robert J. MacDowall[14], Justin C. Kasper[15,16], Anthony W. Case[16], Kelly E. Korreck[16], Davin E. Larson[8], Roberto Livi[8], Michael L. Stevens[16], Phyllis L. Whittlesey[8], and Alexander M. Hegedus[15]
[1] Universities Space Research Association, Columbia, MD 21046, USA; vratislav.krupar@nasa.gov
[2] Heliospheric Physics Laboratory, Heliophysics Division, NASA Goddard Space Flight Center, Greenbelt, MD 20771, USA
[3] Department of Space Physics, Institute of Atmospheric Physics of the Czech Academy of Sciences, Prague 14131, Czech Republic
[4] LESIA, Observatoire de Paris, Université PSL, CNRS, Sorbonne Université, Université de Paris, F-92195 Meudon, France
[5] School of Physics and Astronomy, University of Glasgow, Glasgow G12 8QQ, UK
[6] George Mason University, Fairfax, VA 22030, USA
[7] Physics Department, University of California, Berkeley, CA 94720-7300, USA
[8] Space Sciences Laboratory, University of California, Berkeley, CA 94720-7450, USA
[9] The Blackett Laboratory, Imperial College London, London, SW7 2AZ, UK
[10] School of Physics and Astronomy, Queen Mary University of London, London E1 4NS, UK
[11] Laboratory for Atmospheric and Space Physics, University of Colorado, Boulder, CO 80303, USA
[12] School of Physics and Astronomy, University of Minnesota, Minneapolis, MN 55455, USA
[13] LPC2E, CNRS and University of Orléans, Orléans, France
[14] Solar System Exploration Division, NASA Goddard Space Flight Center, Greenbelt, MD 20771, USA
[15] Climate and Space Sciences and Engineering, University of Michigan, Ann Arbor, MI 48109, USA
[16] Smithsonian Astrophysical Observatory, Cambridge, MA 02138, USA
Received 2019 September 13; revised 2019 December 8; accepted 2019 December 22; published 2020 February 3

Abstract

Radio waves are strongly scattered in the solar wind, so that their apparent sources seem to be considerably larger and shifted than the actual ones. Since the scattering depends on the spectrum of density turbulence, a better understanding of the radio wave propagation provides indirect information on the relative density fluctuations, $\epsilon = \langle \delta n \rangle / \langle n \rangle$, at the effective turbulence scale length. Here, we analyzed 30 type III bursts detected by *Parker Solar Probe* (*PSP*). For the first time, we retrieved type III burst decay times, τ_d, between 1 and 10 MHz thanks to an unparalleled temporal resolution of *PSP*. We observed a significant deviation in a power-law slope for frequencies above 1 MHz when compared to previous measurements below 1 MHz by the twin-spacecraft *Solar TErrestrial RElations Observatory* (*STEREO*) mission. We note that altitudes of radio bursts generated at 1 MHz roughly coincide with an expected location of the Alfvén point, where the solar wind becomes super-Alfvénic. By comparing *PSP* observations and Monte Carlo simulations, we predict relative density fluctuations, ϵ, at the effective turbulence scale length at radial distances between 2.5 and 14 $R_\odot$ to range from 0.22 to 0.09. Finally, we calculated relative density fluctuations, ϵ, measured in situ by *PSP* at a radial distance from the Sun of 35.7 $R_\odot$ during perihelion #1, and perihelion #2 to be 0.07 and 0.06, respectively. It is in a very good agreement with previous *STEREO* predictions ($\epsilon = 0.06$–0.07) obtained by remote measurements of radio sources generated at this radial distance.

Unified Astronomy Thesaurus concepts: Radio astronomy (1338); Radio bursts (1339); Solar flares (1496)

Supporting material: animation

1. Introduction

Type III bursts belong among the strongest radio signals routinely observed by both space-borne and ground-based observatories (Bastian et al. 1998; Miteva et al. 2017). They are generated by electron beams accelerated at reconnection sites of solar flares traveling outward along open magnetic filed lines through the corona and the interplanetary medium (Wild 1950). Along their path, electron beams interact with the background plasma producing radio emissions at the electron plasma frequency, f_{pe} (the fundamental component), and/or at its first harmonic, $2f_{pe}$ (the harmonic component), via the plasma emission mechanism (Ginzburg & Zhelezniakov 1958; Cairns & Robinson 1995; Ergun et al. 1998). Generally, the two components can be distinguished when observed simultaneously, which is rather typical at decametric or shorter wavelengths (Stewart 1974). The fundamental component is usually more intense with 2–3 times higher circular polarization (Dulk & Suzuki 1980). However, it is almost impossible to distinguish the two components in time and frequency, or by polarization for type III bursts at longer wavelengths, which are generated in the interplanetary medium (Reiner et al. 1998; Gopalswamy et al. 2005; Krupar et al. 2015). For rare cases when electron beams are detected in situ at the spacecraft, the initial radiation is almost always the fundamental component, while in the late phases, it may be

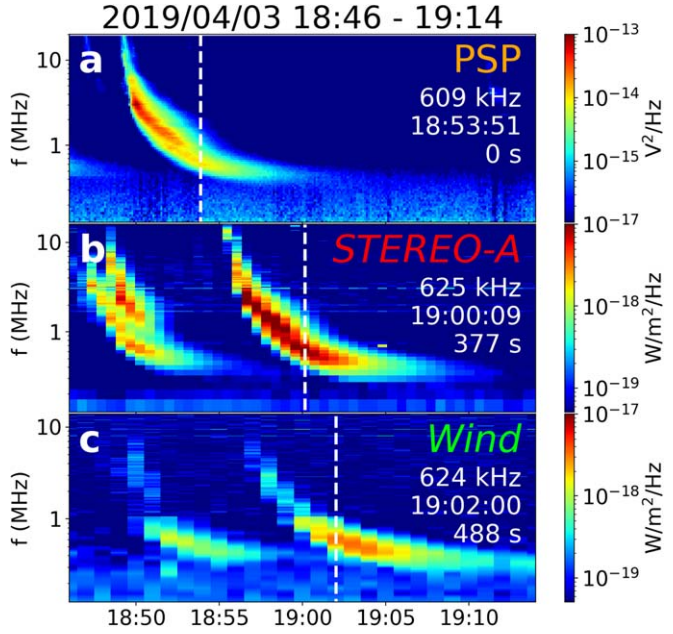

Figure 1. Radio measurements of the 2019 April 3 type III burst. (a) The power spectral density, V_r^2, for *PSP*/RFS. (b) The power flux density, *S*, for *STEREO-A*/WAVES. (c) The power flux density, *S*, for *Wind*/WAVES. White dashed lines indicate times of peak fluxes at 609, 625, and 624 kHz.

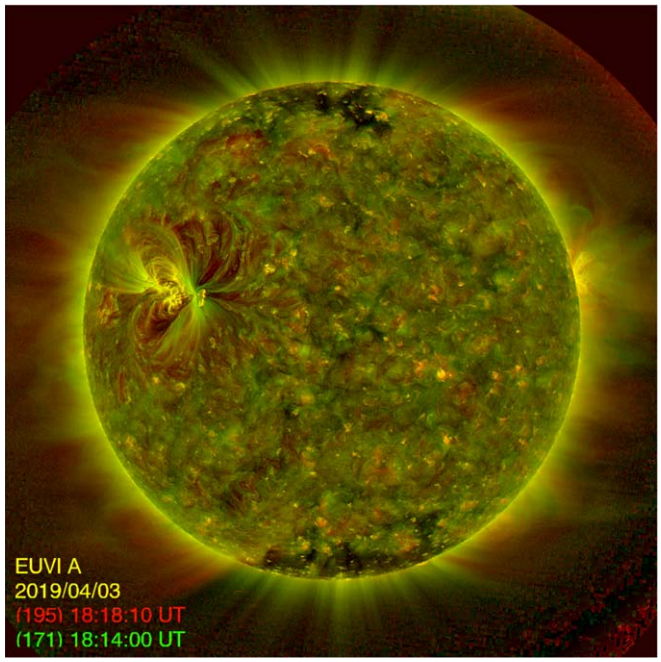

Figure 2. Image of the Sun taken by the *STEREO-A*/SECCHI/EUVI on 2019 April 3 at 18:14:00 UT (171 Å) and 18:18:10 UT (195 Å). Enhanced images for individual wavelength channels are available at http://sd-www.jhuapl.edu/secchi/wavelets/fits/201904/03/. An animation of just the SECCHI/EUVI (195 Å) sequence is available. The animation field of view is zoomed-in to the area around the flare in the upper right quadrant of the full solar image shown in the figure. The video begins on 2019 April 3 at 18:00:30 and ends the same day at 20:05:30. The real-time duration of the video is 2 s. The animation of the solar flare is derotated using the reference time corresponding to the first image (18:00 UT).

(An animation of this figure is available.)

one or another (Dulk et al. 1998). Currently, there is no observational evidence to choose between the fundamental and harmonic component for interplanetary type III bursts.

Type III bursts can be simultaneously detected over a broad range of longitudes, even if their sources are located behind the Sun (Bonnin et al. 2008). Their apparent radio sources lie at considerably larger radial distances than predicted by electron density models (Reiner et al. 2009; Martínez Oliveros et al. 2012). Furthermore, apparent type III burst source sizes are so extended that they may spread over the entire inner heliosphere (Krupar et al. 2014b). These obscure properties are attributed to the scattering of radio waves by electron density inhomogeneities as they propagate from the source region to the observer (Steinberg et al. 1984, 1985; Bastian 1994, 1995; Kontar et al. 2017). The role of refraction and scattering of interplanetary radio emissions can be studied using a geometric optics method and Monte Carlo simulations (Hollweg 1968; Melrose 1980; Thejappa et al. 2007; Thejappa & MacDowall 2008; Kontar et al. 2019).

Recently, Krupar et al. (2018) compared decay times of type III bursts between 125 kHz and 1 MHz observed by the *Solar TErrestrial RElations Observatory* (*STEREO*) spacecraft with results of Monte Carlo simulations. They suggest that the characteristic exponential decay profile of type III bursts could be solely explained by the scattering of the fundamental component between the source and the observer. Krupar et al. (2018) estimated relative electron density fluctuations, $\epsilon = \langle \delta n \rangle / \langle n \rangle$, to be 0.06–0.07 at radial distances from the Sun between 8 and 45 solar radii (1 $R_\odot$ = 695,500 km), where $\langle n \rangle$ represents an average electron density and $\langle \delta n \rangle$ is an average amplitude of variations of an electron density, *n*, from its average value, $\langle n \rangle$.

Here, we primarily examine radio measurements obtained by the *Parker Solar Probe* (*PSP*) mission with a perihelion down to 9.5 $R_\odot$ and aphelion near ~1 au (1 au = 149,598,000 km; Fox et al. 2016). The *PSP*/FIELDS instrument provides with comprehensive measurements of coronal plasma and magnetic field, plasma waves and turbulence, and radio signatures of solar transients (Bale et al. 2016; Pulupa et al. 2017). We use data recorded by the Radio Frequency Spectrometer (RFS), which is a two-channel digital receiver and spectrometer in the FIELDS suite. Specifically, we analyze time–frequency profiles of type III bursts between 0.5 and 10 MHz recorded by the RFS/Low Frequency Receiver (LFR; 64 logarithmically spaced frequency channels between 10.5 kHz and 1.7 MHz with a temporal resolution of 7 s) and the RFS/High Frequency Receiver (HFR; 64 logarithmically spaced frequency channels between 1.3 and 19.2 MHz with a temporal resolution of 7 s). Frequencies above 10 MHz have been excluded from this study due to insufficient time resolution of RFS/HFR. On the other hand, the frequencies below 0.5 MHz are strongly affected by the quasi-thermal noise (QTN; Meyer-Vernet & Perche 1989) due to considerably larger solar wind density near the Sun when compared to 1 au. For a case study, we also use radio data recorded by the *Wind*/WAVES and *STEREO*/WAVES instruments with a temporal resolution of 60 s and 35 s, respectively (Bougeret et al. 1995, 2008). Finally, we investigate solar wind density and bulk velocity retrieved by the *PSP*/Solar Wind Electrons Alphas and Protons (SWEAP) instrument (Kasper et al. 2016).

In this paper, we present a statistical survey of type III burst decay times that can be used to estimate relative electron density fluctuations, ϵ, in the solar wind. In Section 2, we present our analysis of RFS measurements (Section 2.1), its comparison to results of Monte Carlo simulations (Section 2.2), and relative density fluctuations, ϵ, measured in situ by *PSP*

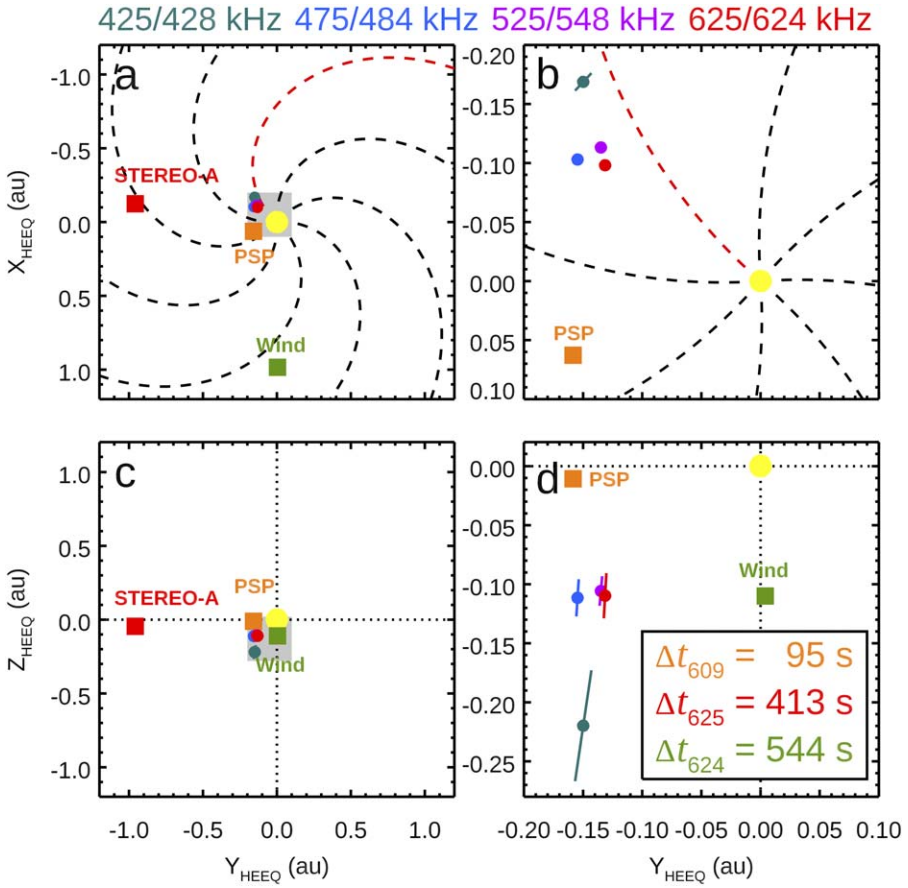

Figure 3. Radio propagation analysis of the 2019 April 3 type III burst. (a)–(d) Triangulated type III burst locations by *STEREO-A* and *Wind* in the XY_{HEEQ} (top) and ZY_{HEEQ} (bottom) planes. Colors denote the frequencies shown on the top. Rectangles show spacecraft locations. Dashed lines indicate Parker spirals (the red one is rooted in the solar flare location). Gray areas in panels (a) and (c) show axis ranges in panels (b) and (d), respectively.

(Section 2.3). Finally, we discuss and summarize our findings in Section 3.

2. Observation and Analysis

2.1. Type III Bursts Measurements

We performed a statistical analysis of 30 type III radio bursts observed by *PSP* during perihelion #2 (2019 April 1–2019 April 10). During this period, radial distances from the Sun ranged from 35.7 to 53.8 $R_{\odot}$. We included only intense, simple, and isolated emissions. We show an analysis of a type III burst from 2019 April 3 when *PSP* was at 68° east from a Sun–Earth line at 36.7 $R_{\odot}$ from the Sun as an example from our list of events. Figure 1(a) displays the power spectral density, *S*, from the RFS/HFR and RFS/LFR instruments using the average auto spectral data of the V1–V2 dipole input channel. *PSP* detected the type III burst with an onset time at about 18:48 UT. The type III burst was also measured by the *Wind*/WAVES and *STEREO-A*/WAVES instruments (Figure 1(b) and 1(c)). During this event, the *Wind* spacecraft was on a Sun–Earth line at 0.99 au from the Sun, whereas *STEREO-A* was at 97° east and 0.97 au from the Sun. We analyzed time delays between peak fluxes for close frequency channels of 609 kHz, 625 kHz, and 624 kHz for *PSP*, *STEREO-A*, and *Wind*, respectively. We selected these channels as higher frequencies were not observed by *Wind*, while a *PSP* radio signal at lower frequencies was affected by QTN. The type III burst was delayed by $\delta t_{\rm STA} = 377$ s and $\delta t_{\rm Wind} = 488$ s between *PSP* and *STEREO-A* and *Wind*, respectively.

A solar flare triggering this emission has been located on the far side of the Sun from a view of the Earth. Hence, we cannot retrieve its intensity and location as spacecraft embarking X-ray imagers orbit the Earth. However, the active region has been observed by *STEREO-A*/Sun Earth Connection Coronal and Heliospheric Investigation/Extreme Ultraviolet Imager (SECCHI/EUVI; Howard et al. 2008). We used the wavelet technique by Stenborg et al. (2008) to produce a composite image for the 171 and 195 Å channels (Figure 2). The coordinates for the footpoint of the loops where some activity is observed at 195Å are [−131°, 6°] in the Stonyhurst–Heliographic longitude and latitude (see the Figure 2 animation).

The favorable configuration of *Wind* and *STEREO-A* allows us to accurately locate the sources of the type III bursts by radio triangulation (Krupar et al. 2014b, 2016). We identified data points that correspond to peak fluxes for four pairs of frequency channels observed by *Wind*/WAVES (428, 484, 548, and 624 kHz) and *STEREO-A*/WAVES (425, 475, 525, and 625 kHz) with signals above background levels. We triangulated the radio sources using wave vector directions during these peak fluxes (Figure 3). Specifically, we consider radio source location to be the closest point between the two wave vectors, and the shortest distance between the wave vectors indicates the error of triangulated source. We also included the Parker spiral rooted in the solar flare site, assuming a solar wind speed of 400 km s^{-1} to illustrate a possible path followed by the electron beam (the red dashed line; Parker 1958). Generally, triangulated source regions of higher

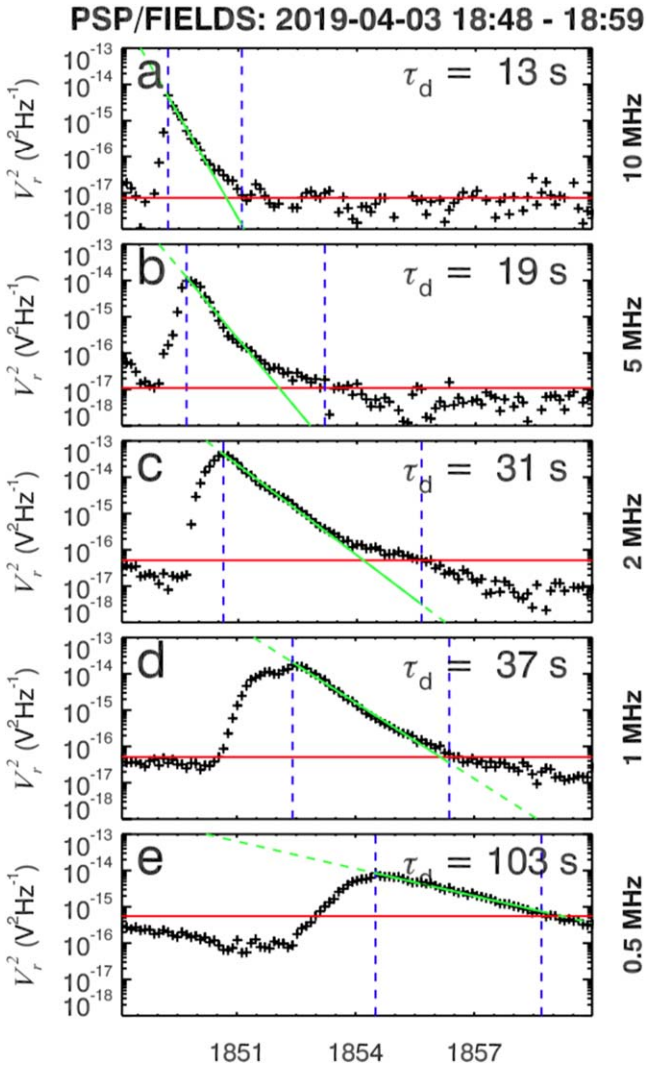

Figure 4. Radio measurements of the 2019 April 3 type III burst. (a)–(e) Fixed frequency light curves of the voltage power spectral density recorded by the RFS instrument for five frequency channels. Red lines show median values in given time intervals. Dashed blue lines denote peak fluxes and last points above median values. Green lines show results of the decay time fitting (Equation (1)).

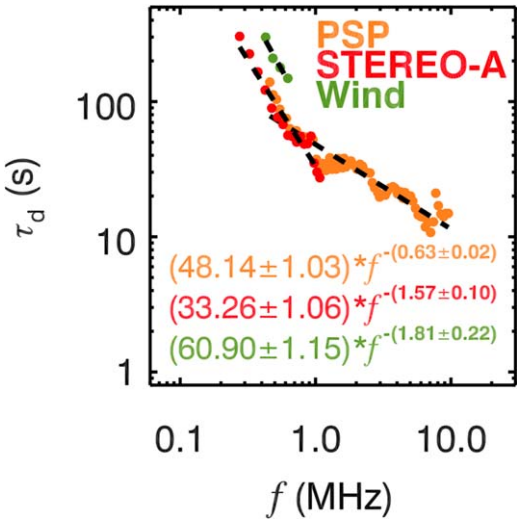

Figure 5. Radio measurements of the 2019 April 3 type III burst. Decay times, τ_d, for *PSP*, *STEREO-A*, and *Wind* as a function of frequency are shown in orange, red, and green, respectively.

frequencies are closer to the Sun. Obtained error bars are noticeable only in the XZ_{HEEQ} plane due to the considerable smaller separation angle between *STEREO-A* and *Wind* in this plane (Figure 3(d)). We also calculated light travel times between the triangulated radio source at 625/624 kHz and all three spacecraft: $\Delta t_{PSP} = 95$ s, $\Delta t_{STA} = 413$ s, and $\Delta t_{Wind} = 544$ s. Using exclusively radio triangulation, we estimated the radio signal delays between *PSP* and *STEREO-A* and *Wind* to be $\delta t_{STA} = \Delta t_{STA} - \Delta t_{PSP} = 318$ s and $\delta t_{Wind} = \Delta t_{Wind} - \Delta t_{PSP} = 449$ s, respectively. These values are comparable with actual delay signal measurements shown in Figure 1 ($\Delta t_{STA} = 377$ s and $\Delta t_{Wind} = 488$ s), which indicates that the radio triangulation technique provides reasonable source locations. Results of the triangulation confirm that the electron beam triggering the type III burst propagates roughly along the Parker spiral field near *PSP*. The signal measured by *STEREO-A*/WAVES was significantly stronger than that measured by *Wind*/WAVES, which is consistent with the radio source located closer to *STEREO-A*/WAVES. Unfortunately, we are unable to perform the radio propagation analysis using *PSP* measurements as the *PSP* effective antenna parameters are not determined yet.

Figure 4 shows fixed frequency light curves of the same event in four frequency channels (0.5, 1, 2, 5, and 10 MHz). The exponential decay of the power spectral density, *S*, over several decades can be identified. For the further analysis, we calculated median values of the power spectral density, *S*, frequency by frequency to estimate the background level (red lines in Figure 4). We analyze data points between the peak time (t_{peak}) and the last value above this level (i.e., between the dashed blue lines in Figure 4). We assume an exponential decay profile of the power spectral density, *S*, that can be described by following equation:

$$S(t) = \frac{I}{\tau_d} \exp\left(\frac{t_{peak} - t}{\tau_d}\right), \quad (1)$$

where *t* is the time and t_{peak} corresponds to the time of the peak power spectral density. Coefficients *I* and τ_d are parameters of a gradient-expansion algorithm used to compute a nonlinear least squares fit. Figure 4 shows the results of this fitting for decay power spectral density profiles in green.

Figure 5 shows type III burst decay times as a function of the frequency for RFS, *STEREO-A*/WAVES, and *Wind*/WAVES. We achieved a very good agreement between RFS and *STEREO-A*/WAVES for overlapping frequency channels (i.e., between 0.5 and 1 MHz). However, decay times retrieved by *Wind*/WAVES are considerably larger. This can be attributed to different emissions' directivity due to relative spacecraft locations, i.e, when *PSP* and *STEREO-A* are nearly along one Parker spiral, while *Wind* is about 90° away in the solar equatorial plane (Figure 3(a)). Next, we assume that the decay times, τ_d, are frequency-dependent as in

$$\tau_d(f) = \alpha f^{\beta}. \quad (2)$$

This model fits the data well for all three spacecraft. We obtained the following spectral indices: $\beta_{PSP} = (-0.63 \pm 0.02)$, $\beta_{STEREO-A} = (-1.57 \pm 0.10)$, and $\beta_{Wind} = (-1.81 \pm 0.22)$. These values were calculated by minimizing the χ^2 error statistic with the 1σ uncertainty estimates. Despite variations in decay times between *STEREO-A*/WAVES and *Wind*/WAVES, the

Table 1
The List of Type III Burst Time–Frequency Intervals

Date Begin (UTC)	Date End (UTC)	Frequency Low (MHz)	Frequency High (MHz)
2019 Apr 1 01:57:00	2019 Apr 1 02:05:00	1.196	9.572
2019 Apr 1 17:10:00	2019 Apr 1 17:17:00	0.545	8.428
2019 Apr 1 20:25:00	2019 Apr 1 20:40:00	0.577	7.725
2019 Apr 2 02:40:00	2019 Apr 2 02:57:00	0.809	9.572
2019 Apr 2 04:44:00	2019 Apr 2 05:00:00	0.514	8.822
2019 Apr 2 09:01:15	2019 Apr 2 09:12:00	0.764	9.572
2019 Apr 3 04:00:00	2019 Apr 3 04:10:00	1.575	9.572
2019 Apr 3 06:00:00	2019 Apr 3 06:10:00	1.566	9.572
2019 Apr 3 09:20:00	2019 Apr 3 09:35:00	0.646	9.572
2019 Apr 3 12:10:00	2019 Apr 3 12:25:00	0.514	9.572
2019 Apr 3 12:35:00	2019 Apr 3 12:50:00	0.514	5.222
2019 Apr 3 16:48:00	2019 Apr 3 17:00:00	0.514	9.572
2019 Apr 3 17:00:00	2019 Apr 3 17:07:00	1.622	5.972
2019 Apr 3 18:48:00	2019 Apr 3 19:00:00	0.514	9.572
2019 Apr 3 21:05:00	2019 Apr 3 21:15:00	1.622	9.572
2019 Apr 3 22:20:00	2019 Apr 3 22:40:00	0.514	9.572
2019 Apr 4 02:35:00	2019 Apr 4 02:50:00	0.646	9.572
2019 Apr 4 05:33:00	2019 Apr 4 05:45:00	0.764	9.572
2019 Apr 4 22:10:00	2019 Apr 4 22:30:00	0.514	9.572
2019 Apr 4 22:30:00	2019 Apr 4 22:40:00	0.646	9.572
2019 Apr 5 03:25:00	2019 Apr 5 03:40:00	0.514	9.572
2019 Apr 5 04:32:00	2019 Apr 5 04:42:00	0.855	9.572
2019 Apr 5 10:52:00	2019 Apr 5 11:00:00	1.481	9.572
2019 Apr 5 16:52:00	2019 Apr 5 17:15:00	0.514	9.572
2019 Apr 5 17:06:00	2019 Apr 5 17:30:00	0.514	8.072
2019 Apr 6 07:45:00	2019 Apr 6 07:59:00	0.514	9.572
2019 Apr 6 09:40:00	2019 Apr 6 09:59:00	0.514	9.572
2019 Apr 6 10:40:00	2019 Apr 6 10:59:00	0.514	9.572
2019 Apr 7 09:50:00	2019 Apr 7 10:00:00	0.957	9.572
2019 Apr 10 14:25:00	2019 Apr 10 14:45:00	1.566	9.572

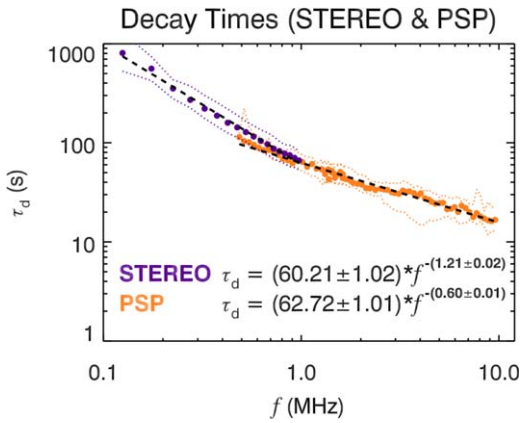

Figure 6. Results of the statistical survey of 152 and 30 type III radio bursts for *STEREO* and *PSP*. Median values of decay times, τ_d, for *STEREO* and *PSP* as a function of frequency are shown in purple and orange, respectively. Error bars are in the 25th/75th percentiles. Dashed black lines represent results of power-law fitting for the two data sets separately (Equation (2)).

obtained spectral indices are rather similar. On the other hand, β_{PSP} is significantly larger due to contributions by frequency channels between 1 and 10 MHz, which are not covered by *STEREO-A*/WAVES and *Wind*/WAVES.

We performed the above-described analysis of the exponential decay times, τ_d, on 30 type III bursts observed by *PSP* during perihelion #2 case by case. We provide the list of type III burst time–frequency intervals, which can be used for further investigation by the community (Table 1). Figure 6 displays median values of decay times, τ_d, as a function of the frequency. We assume that the decay times, τ_d, are frequency-dependent as a power law (Equation (2)). The model fits the data very well. We obtained the spectral indices, β_{PSP}, of -0.60 ± 0.1.

2.2. Monte Carlo Simulations

Thejappa et al. (2007) developed a Monte Carlo simulation code to investigate a role of refraction and scattering on the propagation of interplanetary radio emissions with isotropic sources when observed by spacecraft at 1 au. For the refraction, the solar wind electron density model of Bougeret et al. (1984) was used ($n \sim r^{-2.10}$). For the scattering, Thejappa et al. (2007) assumed the power spectrum of electron density fluctuations in the solar wind, P_n, in the inertial range to be proportional to the Kolmogorov spectrum. The relative electron density fluctuations, ϵ, were set to be 0.07. We modified the Monte Carlo technique of Thejappa et al. (2007) to simulate arrival times, t_{MC}, of radio emissions to 35.7 $R_\odot$ (i.e., a radial distance of *PSP* during perihelion #2). Contrary to Thejappa et al. (2007), we used a 10 times finer simulation grid; variable values of the inner scale, l_i (Coles & Harmon 1989); and the Sittler & Guhathakurta (1999) density model, which works better for frequencies above 1 MHz.

Figure 7 shows histograms of simulated arrival times, t_{MC}, of rays generated at 2 MHz for four levels of the relative electron density fluctuations ($\epsilon = 0.05$, 0.10, 0.15, and 0.20). We assumed the presence of the fundamental component only in

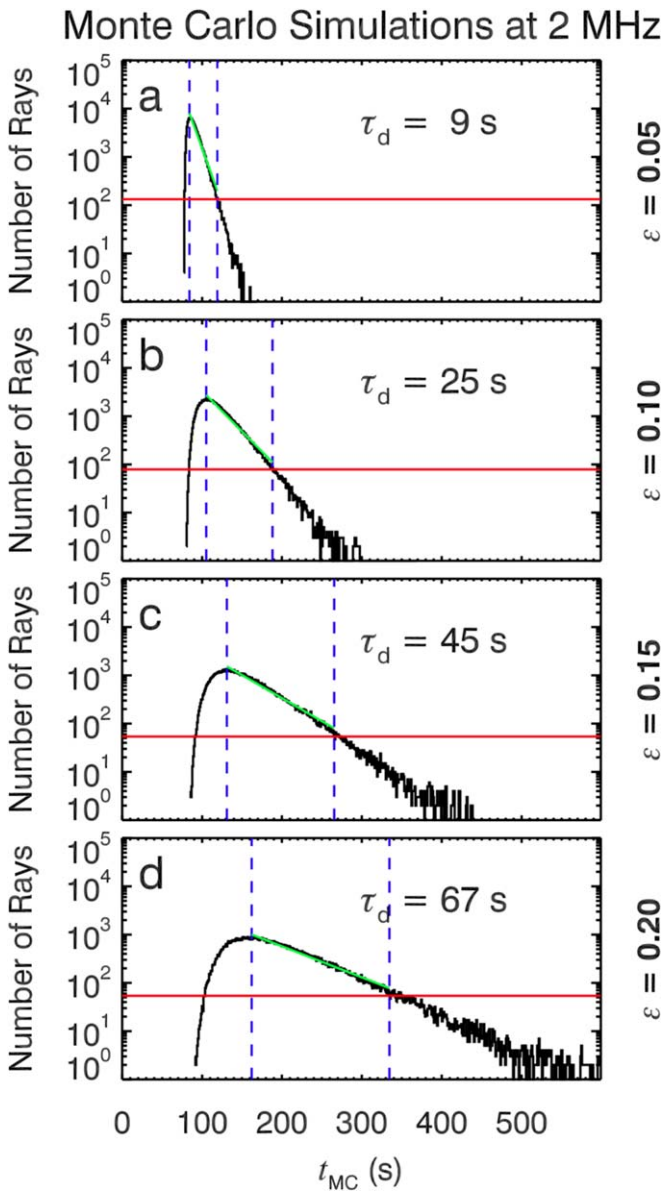

Figure 7. Results of Monte Carlo simulations at 2 MHz. (a)–(d) Histograms of simulated time arrivals, t_{MC}, for various levels of relative electron density fluctuations, ϵ. Red lines show median values. Dashed lines denote peak fluxes and last points above median values. Green lines show results of decay time fittings (Equation (1)).

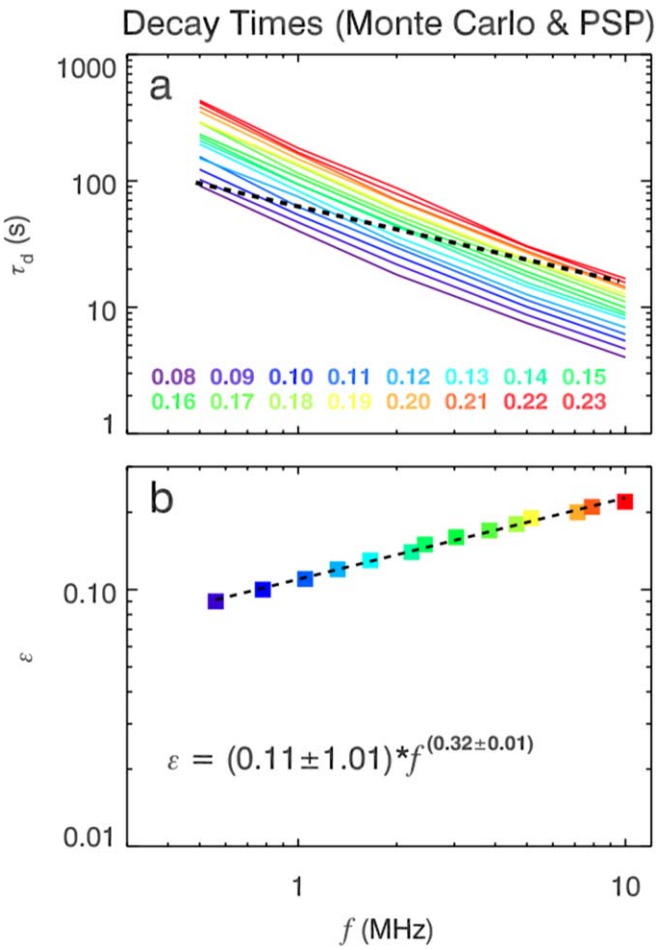

Figure 8. Comparison of Monte Carlo simulations and *PSP* observations. (a) Simulated decay times, τ_d, as a function of the frequency for 16 levels of relative density fluctuations, ϵ, in color. A dashed black line shows fitting results from *PSP* (Figure 6). (b) Relative density fluctuations, ϵ, as a function of the frequency retrieved from intersections between Monte Carlo simulations and *PSP* observations. A dashed black line represents results of power-law fittings.

accordance with Krupar et al. (2018). We identify similar exponential decay profiles as for the RFS measurements in Figure 4. We assume that the number of rays can be directly compared to the power spectral density, S. We applied the same approach as for RFS data to derive the decay times, τ_d, from these histograms (Figure 4). We found that the exponential model described by Equation (1) is in a good agreement with simulated data. A direct comparison between *PSP* observations (Figure 4(c)) and Monte Carlo simulations (Figures 7(b) and 7(c)) suggests that there are relative electron density fluctuations, ϵ, at the effective turbulence scale length to be between 0.10 and 0.15 for emission generated at 2 MHz.

Next, we performed the Monte Carlo simulations for five frequency channels (0.5, 1, 2, 5, and 10 MHz) and 16 levels of the relative electron density fluctuations, ϵ, between 0.08 and 0.23. Figure 8(a) shows simulated and observed decay times, τ_d, versus the frequency, f. While previous analysis of the *STEREO* data by Krupar et al. (2018) suggested that observed decay times, τ_d, can be explained by scattering due to nearly constant relative electron density fluctuations ($\epsilon = 0.06$–0.07), we need variable values to interpret the *PSP* data ($\epsilon = 0.09$–0.22). Figure 8(a) displays relative density fluctuations, ϵ, as a function of the frequency. The higher frequencies require larger levels of ϵ to explain observed decay times, τ_d, by *PSP*. We found that this relation can be described by a power law as

$$\epsilon(f) = \alpha f^{\beta}. \quad (3)$$

Next, we converted frequencies to radial distances using the Sittler & Guhathakurta (1999) density model (Figure 9). The obtained relation can be described by a power-law type with a spectral index of -0.55 ± 0.01 for radial distances from 2.4 $R_\odot$ up to 13.9 $R_\odot$. We note that *STEREO* results between 125 kHz and 1 MHz (i.e., from 8.4 $R_\odot$ up to 45.1 $R_\odot$) suggest nearly constant relative density fluctuations of $\epsilon = 0.06$–0.07 at the effective turbulence scale length (Krupar et al. 2018).

2.3. Density Fluctuations

Finally, we compared predicted relative density fluctuations by *STEREO* (Krupar et al. 2018) and the measured ones by

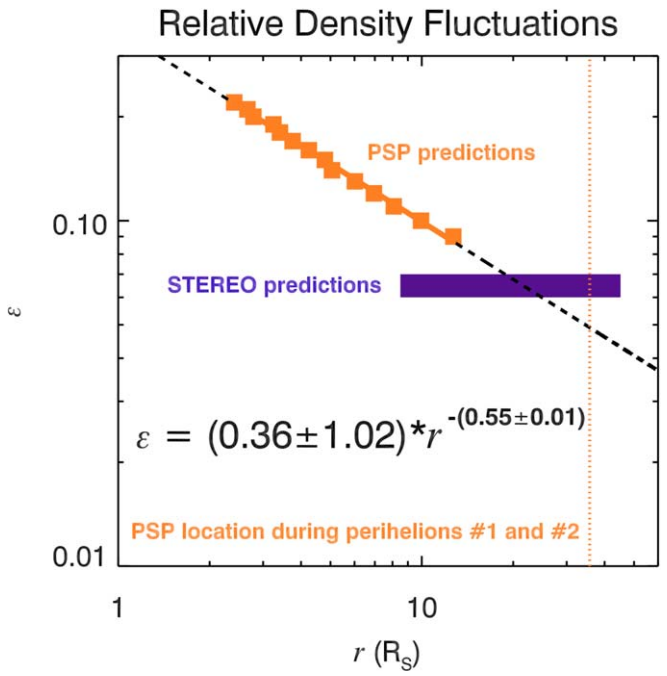

Figure 9. Results of Monte Carlo simulations and *PSP* observations. Relative density fluctuations, ϵ, from Figure 8(b) as a function of radial distance r are denoted by orange squares. A solid black line represents results of power-law fittings. Predicted relative density fluctuations, ϵ, by *STEREO* are shown in purple. A dotted orange line indicates the radial distance of *PSP* during perihelions #1 and #2.

PSP/SWEAP during perihelions #1 and #2. Specifically, we use density and velocity measurements based on the proton moments from the Faraday cup. We calculated median values of the plasma density and bulk velocity during periods that were 12 hr before and 12 hr after the closest approaches (Figures 10(a)–10(d)). Obtained plasma densities correspond to local plasma frequencies of $f_p = 137$ kHz and $f_p = 86$ kHz for perihelions #1 and #2, respectively. The Monte Carlo technique assumes the fundamental emission to be generated at $1.05f_p$, resulting in $f = 143$ kHz and $f = 91$ kHz. Next, we retrieve effective spatial scales, $l_{\rm eff}$, for these frequencies using an empirically derived model of the inner and outer scales of the electron density fluctuations. We compared these spatial scales with median values of plasma bulk velocities to obtain effective temporal scales of the density turbulence, $t_{\rm eff}$. Next, we calculated relative density fluctuations, ϵ, as a function of the timescale, t, between 10 s and 100 minutes:

$$\epsilon(t) = \frac{\langle |n - \langle n \rangle_t| \rangle_t}{\langle n \rangle_t}. \quad (4)$$

For timescales corresponding to the effective turbulence scale length in our Monte Carlo simulation technique, we obtained $\epsilon = 0.07$ and $\epsilon = 0.06$ for perihelions #1 and #2, respectively. It is in very good agreement with relative density fluctuations of $\epsilon = 0.06$–0.07 predicted by Krupar et al. (2018).

3. Discussion and Summary

While type III bursts have been been observed for almost 70 years, a proper model to explain their obscure properties is still missing. *PSP*/RFS is the state-of-the-art instrument that allows us to investigate interplanetary solar radio bursts with an unprecedented time resolution near the Sun. For the first time, we can accurately retrieve type III burst decay times for frequencies between 1 and 10 MHz to remotely probe solar wind turbulence near the Sun. Although PSP/RFS accumulated a wealth of data during the first two perihelions, type III bursts were almost exclusively observed only during perihelion #2 despite the ongoing solar minimum.

We show an analysis of a type III burst that occurred on 2019 April 3 during perihelion #2 (Figure 1), which was associated with the active region at $[-131°, 6°]$ in the Stonyhurst–Heliographic longitude and latitude (Figure 2). We note that this active region was responsible for a majority of solar activity during perihelion #2. The simple type III burst was also observed couple minutes later by *STEREO-A* and *Wind*, which allowed us to compare signal delays between the three spacecraft. We have localized radio sources using a triangulation technique applied to *STEREO-A*/Waves and *Wind*/Waves measurements (Figure 3). Triangulated radio sources lie near the modeled Parker spiral rooted in the active region. The results from the radio triangulation and time delay analysis confirm that this radio emission is related to the active region. We analyzed RFS fixed frequency light curves for five frequency channels (Figure 4; 0.5, 1, 2, 5, and 10 MHz). We observed the characteristic exponential decay profile for all frequency channels. However, the fit does not perform well for late phases at higher frequencies and a clear hardening of the profile can be recognized. This effect is probably related to underestimating of the background level for the exponential decay fit at higher frequencies. While the type III burst is above the estimated background level for almost six minutes at 0.5 MHz, it is only around two minutes at 10 MHz. Consequently, the background level at 10 MHz on the same 11 minute time interval is relatively lower when compared to measurements at 0.5 MHz. Other explanation would be the presence of the harmonic component and/or another weaker type III burst. Nevertheless, these deviations in late phases are of minor importance to affect calculated decay times since obtained values predominantly rely on data points succeeding peak fluxes, where the exponential decay fit performs very well. Figure 5 shows a comparison of decay times observed by all three spacecraft. Despite different radial distances of *PSP* and *STEREO-A* from the Sun, obtained results are comparable for overlapping frequencies as the two spacecraft lie approximately on the same Parker spiral. This indicates that scattering—if responsible for long exponential decays—occurs primarily near sources, and radio waves propagate along straight lines afterward. Nonetheless, the exponential decay exhibits a clear hardening above 1 MHz, which will be discussed later. We note that the hardening would be even more pronounced if the late phases in Figure 4 are included. On the other hand, decay times observed by *Wind* are considerably longer, perhaps due to larger longitudinal separation with the active region. However, the slope of the power-law fit is similar to *STEREO-A*. A comparison of decay times from widely separated spacecraft may provide additional information for radio triangulation and/or a time delay analysis to complement radio source localization.

We investigated a large number of type III bursts in order to statistically retrieve their exponential decay times, τ_d, as a function of the frequency, f (Figure 6). Using the power-law model, we obtain a spectral index, $\beta_{\rm PSP}$, of -0.60 ± 0.01. Recently, Krupar et al. (2018) performed a similar analysis of 152 type III bursts between 125 kHz and 1 MHz observed by the *STEREO* spacecraft located at 1 au. The obtained spectral index is about two times smaller than *PSP* ($\beta_{\rm STEREO} = -1.21 \pm 0.01$).

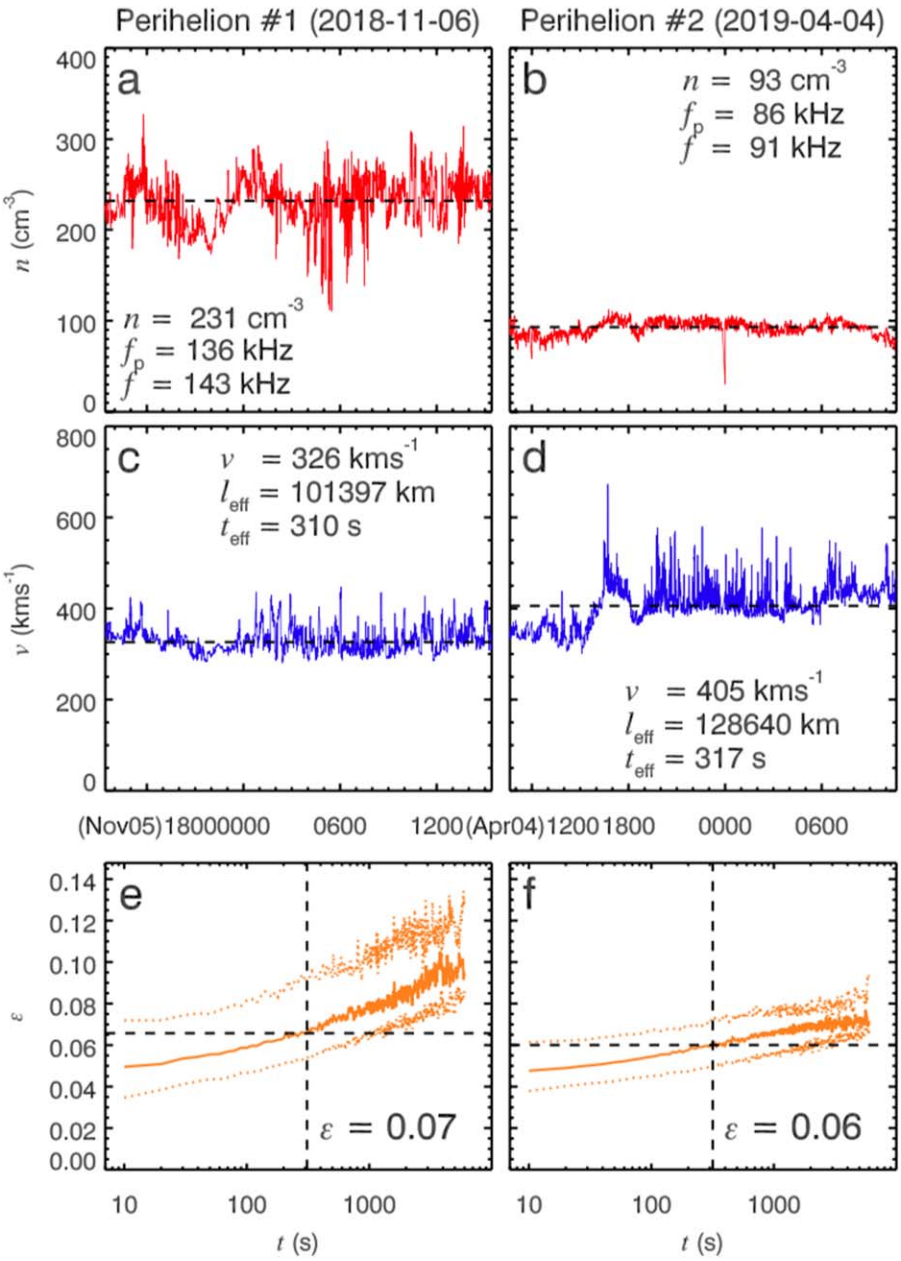

Figure 10. *PSP* plasma measurements 12 hr before and 12 hr after perihelion #1 (left) and perihelion #2 (right). (a) and (b) Plasma density. (c) and (d) Bulk velocity. Dashed black lines show median values. (e) and (f) Median values of relative density fluctuations, ϵ, as a function of temporal scale t. Error bars are in the 25th/75th percentiles. Dashed black lines correspond to the effective scales of Monte Carlo simulations for frequencies of 143 and 91 kHz obtained from plasma parameters obtained during perihelions #1 and #2.

However, statistical results between 0.5 and 1 MHz by both *PSP* (30 events detected in 2019 April at ∼0.17 au) and *STEREO* (152 events measured between 2007 May and 2013 February at ∼1 au are comparable. If one assumes that exponential decay is caused by scattering, then it confirms that scattering is only important close to radio sources and that later type III bursts propagate along straight lines. The Sittler & Guhathakurta (1999) density model suggests that 1 MHz—where the slope changes between *STEREO* and *PSP*—corresponds to a radial distance of ∼8 $R_\odot$ (the fundamental component) or ∼14 $R_\odot$ (the harmonic component), where the solar wind speed typically exceeds the Alfvén speed and the solar wind become super-Alfvénic; the solar wind is no longer in contact with the Sun since Alfvén waves cannot travel back to the Sun and type III burst properties change around 1 MHz as the ambient plasma evolves significantly. Moreover, type III bursts statistically also exhibit a maximum of the power spectral density around 1 MHz (Krupar et al. 2014a). Furthermore, it is also possible that we rather observe the fundamental component below 1 MHz, while the harmonic component is dominant above 1 MHz. If it is the case, variations in exponential decay times within one single type III burst can be used to distinguish one component from another.

We implemented a Monte Carlo simulation technique to study a role of scattering for type III burst decay times (Figure 7). We assumed a presence of the fundamental component only since the used Monte Carlo simulation technique does not perform well for the harmonic one. Specifically, Krupar et al. (2018) showed that distributions of simulated arrival times of the harmonic component are very narrow with short onset times, which is inconsistent with type

III burst observations. Moreover, the following assumptions have been included in the Monte Carlo code: (1) an isotropic point source, (2) the Sittler & Guhathakurta (1999) density model, (3) a power-law distribution of density fluctuations, (4) empirically modeled inner and outer scales, and (5) a constant value of isotropic density fluctuations. Obviously, these simplifications affect our analysis and can be improved in the future. For example, a finite size dipole/quadrupole emission pattern would probably slightly increase modeled decay times. A variable anisotropic density fluctuation model would work better for radio emission generated near the Sun.

From the arrival times, we calculated the decay times, τ_d, that we compare to those observed by RFS (Figure 8). As scattering plays a significant role near radio sources only, we may assume variable levels of ϵ when comparing *PSP* observations with Monte Carlo simulations for each frequency separately. Our results suggest that the exponential decay of the observed power spectral density can be explained by the scattering of a radio signal by density inhomogeneities in the solar wind. Obtained relative electron density fluctuations, ϵ, are 0.09–0.22 at the effective turbulence scale length. We note that this range depends on our assumptions of the effective scale, $l_{\rm eff}$, of the electron density fluctuations near actual radio sources. Predicted electron density fluctuations increase closer to the Sun below the Alfvén point (Figure 9). Nonetheless, *STEREO* observations indicate constant density fluctuations above the Alfvén point (Krupar et al. 2018). A possible explanation of this discrepancy would be that solar wind turbulence is primarily formed near the Sun, while it remains frozen in the solar wind once beyond the Alfvén point.

Finally, we analyzed plasma parameters measured in situ by *PSP* during perihelions #1 and #2 to exploit unique observations near the Sun (Figure 10). Our results suggest that relative density fluctuations, ϵ, are 0.06–0.07 at the effective turbulence scale length in our Monte Carlo simulation technique, which is confirmed previous predictions by Krupar et al. (2018). The main results of this study have been obtained by a statistical analysis of 30 type III bursts observed by *PSP* during perihelion #2, by Monte Carlo modeling of radio wave propagation in the solar wind, and by an analysis of in situ plasma measurements during perihelions #1 and #2. We have concluded that:

1. Type III burst decay times between 0.5 and 1 MHz are statistically comparable at ~0.17 and ~1 au, which confirms that scattering plays a major role in radio wave propagation near sources only.
2. Type III burst decay times between 1 and 10 MHz are statistically longer than expected based on previous observations at lower frequencies. This can be explained either by different ambient plasma parameters above the Alfvén point or because we preferably observe the harmonic component above 1 MHz.
3. If the latter is true, variations in exponential decay times can be used to distinguish fundamental and harmonic components within one single type III burst.
4. By comparing *PSP* observations and Monte Carlo simulations, we predicted relative density fluctuations, ϵ at, radial distances between 2.5 and 14 $R_\odot$ to range from 0.22 and 0.09.
5. Observed relative density fluctuations, ϵ, at a radial distance from the Sun of 35.7 $R_\odot$ were 0.06–0.07.

Note, however, that predicted relative density fluctuations, ϵ, are based on an assumption that we primarily observe the fundamental component of type III bursts only as the used Monte Carlo technique does not perform well for the harmonic component (Krupar et al. 2018).

The authors would like to thank the many individuals and institutions who contributed to making *PSP*, *STEREO*, and *Wind* possible. V.K. acknowledges support by an appointment to the NASA postdoctoral program at the NASA Goddard Space Flight Center administered by Universities Space Research Association under contract with NASA and the Czech Science Foundation grant 17-06818Y. O.K. thanks support of the Czech Science Foundation grant 17-06065S. E.P.K. was supported by an STFC consolidated grant ST/P000533/1. S.D.B. acknowledges the support of the Leverhulme Trust Visiting Professorship program. Data access and processing was performed using SPEDAS (Angelopoulos et al. 2019). All data is publicly available at https://spdf.gsfc.nasa.gov/ and https://umbra.nascom.nasa.gov/.

ORCID iDs

Vratislav Krupar https://orcid.org/0000-0001-6185-3945
Adam Szabo https://orcid.org/0000-0003-3255-9071
Milan Maksimovic https://orcid.org/0000-0001-6172-5062
Oksana Kruparova https://orcid.org/0000-0002-1122-6422
Eduard P. Kontar https://orcid.org/0000-0002-8078-0902
Laura A. Balmaceda https://orcid.org/0000-0003-1162-5498
Xavier Bonnin https://orcid.org/0000-0003-4217-7333
Stuart D. Bale https://orcid.org/0000-0002-1989-3596
Marc Pulupa https://orcid.org/0000-0002-1573-7457
David M. Malaspina https://orcid.org/0000-0003-1191-1558
John W. Bonnell https://orcid.org/0000-0002-0675-7907
Peter R. Harvey https://orcid.org/0000-0002-6938-0166
Keith Goetz https://orcid.org/0000-0003-0420-3633
Thierry Dudok de Wit https://orcid.org/0000-0002-4401-0943
Robert J. MacDowall https://orcid.org/0000-0003-3112-4201
Justin C. Kasper https://orcid.org/0000-0002-7077-930X
Anthony W. Case https://orcid.org/0000-0002-3520-4041
Kelly E. Korreck https://orcid.org/0000-0001-6095-2490
Davin E. Larson https://orcid.org/0000-0001-5030-6030
Roberto Livi https://orcid.org/0000-0002-0396-0547
Michael L. Stevens https://orcid.org/0000-0002-7728-0085
Phyllis L. Whittlesey https://orcid.org/0000-0002-7287-5098
Alexander M. Hegedus https://orcid.org/0000-0001-6247-6934

References

Angelopoulos, V., Cruce, P., Drozdov, A., et al. 2019, SSRv, 215, 9
Bale, S. D., Goetz, K., Harvey, P. R., et al. 2016, SSRv, 204, 49
Bastian, T. S. 1994, ApJ, 426, 774
Bastian, T. S. 1995, ApJ, 439, 494
Bastian, T. S., Benz, A. O., & Gary, D. E. 1998, ARA&A, 36, 131
Bonnin, X., Hoang, S., & Maksimovic, M. 2008, A&A, 489, 419
Bougeret, J. L., Goetz, K., Kaiser, M. L., et al. 2008, SSRv, 136, 487
Bougeret, J.-L., Kaiser, M. L., Kellogg, P. J., et al. 1995, SSRv, 71, 231
Bougeret, J.-L., King, J. H., & Schwenn, R. 1984, SoPh, 90, 401
Cairns, I. H., & Robinson, P. A. 1995, ApJ, 453, 959
Coles, W. A., & Harmon, J. K. 1989, ApJ, 337, 1023

Dulk, G. A., Leblanc, Y., Robinson, P. A., Bougeret, J.-L., & Lin, R. P. 1998, JGR, 103, 17223
Dulk, G. A., & Suzuki, S. 1980, A&A, 88, 203
Ergun, R. E., Larson, D., Lin, R. P., et al. 1998, ApJ, 503, 435
Fox, N. J., Velli, M. C., Bale, S. D., et al. 2016, SSRv, 204, 7
Ginzburg, V. L., & Zhelezniakov, V. V. 1958, SvA, 2, 653
Gopalswamy, N., Aguilar-Rodriguez, E., Yashiro, S., et al. 2005, JGRA, 110, 12S07
Hollweg, J. V. 1968, AJ, 73, 972
Howard, R. A., Moses, J. D., Vourlidas, A., et al. 2008, SSRv, 136, 67
Kasper, J. C., Abiad, R., Austin, G., et al. 2016, SSRv, 204, 131
Kontar, E. P., Chen, X., Chrysaphi, N., et al. 2019, ApJ, 884, 122
Kontar, E. P., Yu, S., Kuznetsov, A. A., et al. 2017, NatCo, 8, 1515
Krupar, V., Eastwood, J. P., Kruparova, O., et al. 2016, ApJL, 823, L5
Krupar, V., Kontar, E. P., Soucek, J., et al. 2015, A&A, 580, A137
Krupar, V., Maksimovic, M., Kontar, E. P., et al. 2018, ApJ, 857, 82
Krupar, V., Maksimovic, M., Santolik, O., et al. 2014a, SoPh, 289, 3121
Krupar, V., Maksimovic, M., Santolik, O., Cecconi, B., & Kruparova, O. 2014b, SoPh, 289, 4633
Martínez Oliveros, J. C., Lindsey, C., Bale, S. D., & Krucker, S. 2012, SoPh, 279, 153
Melrose, D. B. 1980, SSRv, 26, 3
Meyer-Vernet, N., & Perche, C. 1989, JGR, 94, 2405
Miteva, R., Samwel, S. W., & Krupar, V. 2017, JSWSC, 7, A37
Parker, E. N. 1958, ApJ, 128, 677
Pulupa, M., Bale, S. D., Bonnell, J. W., et al. 2017, JGRA, 122, 2836
Reiner, M. J., Goetz, K., Fainberg, J., et al. 2009, SoPh, 259, 255
Reiner, M. J., Kaiser, M. L., Fainberg, J., & Stone, R. G. 1998, JGR, 103, 29651
Sittler, E. C., Jr., & Guhathakurta, M. 1999, ApJ, 523, 812
Steinberg, J. L., Hoang, S., & Dulk, G. A. 1985, A&A, 150, 205
Steinberg, J. L., Hoang, S., Lecacheux, A., Aubier, M. G., & Dulk, G. A. 1984, A&A, 140, 39
Stenborg, G., Vourlidas, A., & Howard, R. A. 2008, ApJ, 674, 1201
Stewart, R. T. 1974, SoPh, 39, 451
Thejappa, G., & MacDowall, R. J. 2008, ApJ, 676, 1338
Thejappa, G., MacDowall, R. J., & Kaiser, M. L. 2007, ApJ, 671, 894
Wild, J. P. 1950, AuJPH, 3, 541